Dynamic phase behavior of amorphous solid dispersions revealed with *in situ* stimulated Raman scattering microscopy

Teemu Tomberg[1], Ilona Hämäläinen[1,2], Clare Strachan*[1], Bert van Veen[2]

[1]Division of Pharmaceutical Chemistry and Technology, Faculty of Pharmacy, University of Helsinki, Finland

[2]Pharmaceutical Sciences, Orion Corporation, Finland

*Phone: +358503185341, +358294159736, Email: clare.strachan@helsinki.fi, Address: PL 56 (Viikinkaari 5 E), 00014 University of Helsinki, Finland

Table of Contents/Abstract Graphic

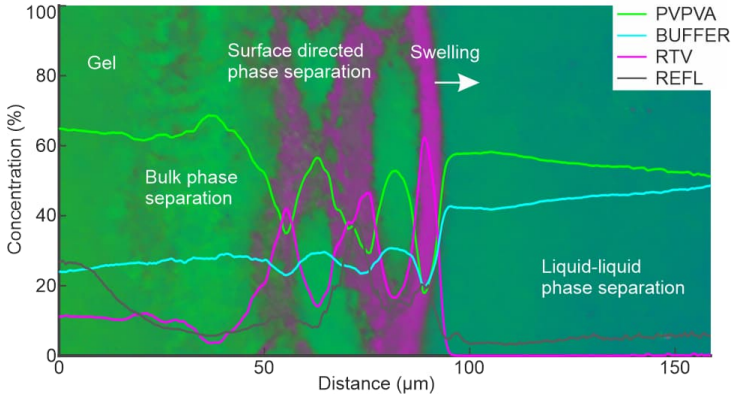

Abstract

This study reports the application of *in situ* stimulated Raman scattering (SRS) microscopy for real-time chemically-specific imaging of dynamic phase phenomena in amorphous solid dispersions (ASD). Using binary ritonavir and poly(vinylpyrrolidone-vinyl acetate) films with different drug loadings (0-100% w/w) as model systems, we employed SRS microscopy with fast spectral focusing to analyze ASD behavior upon contact with dissolution medium. Multivariate unmixing of the SRS spectra allowed changes in the distributions of the drug, polymer and water to be (semi-)quantitatively imaged in real time, both in the film and the adjacent dissolution medium. The SRS analyses were further augmented with complementary correlative sum frequency generation and confocal reflection, for additional crystallinity and phase sensitivity. In the ASDs with drug loadings of 20, 40 and 60% w/w, the water penetration front within the film, followed by both surface-directed and bulk phase separation in the film were apparent, but differed quantitatively. Additionally, drug-loading and phase dependent polymer and drug release behavior was imaged, and liquid-liquid phase separation was observed for the 20% drug loading ASD. Overall, SRS microscopy with fast spectral focusing provides quantitative insights into water-induced ASD phase phenomena, with chemical, solid-state, temporal and spatial resolution. These insights are important for optimal ASD formulation development.

Keywords

Amorphous solid dispersion; stimulated Raman scattering microscopy; amorphous-amorphous phase separation; poorly soluble; dissolution; imaging

Introduction

Amorphous solid dispersions (ASD) represent a key enabling technology to enhance the dissolution of poorly soluble drugs and thus ensure sufficient bioavailability and therapeutic effectiveness [1, 2]. In its most common form, the drug is molecularly and homogenously dispersed in an amorphous, water-soluble polymer as a glassy solution, at a defined drug-to-polymer ratio. The polymer can provide multiple benefits: during storage it inhibits crystallization of the drug, while during drug release itself, the polymer both enhances wettability and dissolution of the drug, and inhibits crystallization (spring and parachute effect) [3]. Despite successful examples of amorphous solid dispersions on the market, development of such formulations is still highly challenging, not least due to difficulties in understanding and simultaneously optimizing processability, stability during storage and drug release upon administration [2].

As well as selection of a suitable polymer and processing method, the drug-to-polymer ratio is critically important. While a drug loading below the solubility limit ensures a thermodynamically stable ASD (at a given temperature and humidity/water content), higher drug loadings are often required and instead kinetic stabilization by the polymer must be relied upon to prevent undesirable physical changes during storage and administration [3]. Traditionally, inhibition of drug crystallization during storage and drug release has been considered the most important parameters to control during the development of ASDs [3-5]. However, more recently, amorphous-amorphous phase separation (AAPS) has also been revealed to be critically important. Substantial progress has been made over the last few years into understanding such phase separation, both during storage (as a function of temperature and relative humidity) [6], and more recently during drug release in aqueous media [2].

A series of impactful studies in the last few years, in particular by the research groups of Taylor and Sadowksi and their collaborators, has revealed the critically important role of AAPS of ASDs in aqueous media can play in mediating drug release, particularly as a function of drug loading [7-11]. The studies have shown that below a threshold drug loading value, typically between 5 and 40% (depending on the drug, polymer and drug release conditions), the dissolution of the ASD is driven by the polymer solubility in the aqueous media and drug and polymer release is congruent (i.e. the drug and polymer release concurrently at the same rate). In this scenario, the film may remain as a single phase during drug release, or, water-driven AAPS may occur faster than dissolution of the ASD, but with the result of the drug-rich phase being disperse (i.e. the drug rich phase exists as droplets/particles within the continuous polymer-rich phase). However, at higher drug loadings, AAPS can occur within and at the surface of the ASD faster than dissolution of the ASD, in which the drug-rich phase becomes the continuous (percolating) phase and the polymer-rich phase is discrete. In this scenario, the much lower solubility of the amorphous drug itself then dictates release, and to a greater or lesser extent, also the polymer. The consequence of such phase separation can be dramatic, with the drug (and polymer) release often dropping to negligible levels. This has been described as the 'falling-off-the-cliff' effect [7].

In situ analysis of phase separation behavior during drug release is challenging but can be highly informative. Yang and coworkers [7] probed the role of phase separation and morphology on release behavior of ritonavir-PVPVA ASD tablets in buffer with different drug loadings at 10% intervals. They employed hydrophobic and hydrophilic fluorescent marker molecules and *in situ* confocal fluorescence imaging to indirectly track gel layer development from the matrix-buffer interface in real time, together with associated drug-polymer phase separation. They observed rapid phase separation into separate drug and polymer rich domains. At lower drug loadings (10 and 20%), discrete drug rich domains formed and

were associated with polymer-driven release in which the drug and polymer released congruently, while at higher drug loadings (30% and 40%), continuous drug-rich domains were formed at the matrix surface that dramatically inhibited release of both the drug and polymer. Fluorescence imaging with the same marker molecules has been employed to characterize phase separation of an expanding array of APIs and polymers in ASDs, with efforts made to identify the physicochemical properties driving phase separation behavior and associated alterations in drug and polymer dissolution [8, 9, 11].

While these studies demonstrate that substantial insights into the phase behavior of ASDs can be gained from the use of fluorescent marker molecules, and the instrumentation is highly accessible, direct *in situ* chemically- and solid-state specific optical imaging of the API(s) and excipients themselves, at equally good spatial resolution, would have benefits. Firstly, it would allow the sample to be analyzed as is and without any manipulation as such, and naturally avoids having to rely on the assumption that the marker molecules associate with the target molecules as predicted. Secondly, the distribution of numerous components in the system, including water, could potentially be (semi-)quantitatively imaged. Finally, a suitable direct imaging technique could also provide solid-state specificity. Attenuated total reflection Fourier transform infrared (ATR-FTIR) macroscopic imaging has been developed by the research group of Kazarian in particular, to quantitively image ASD interactions with dissolution media, including water ingress, drug and polymer dissolution, and drug crystallization in ASDs. They have also coupled the technique with magnetic resonance imaging (MRI) and Raman microscopy (over a much smaller region), to further image water ingress in 3D and drug crystallization, respectively [5]. While the ATR-FTIR imaging has provided tremendous insights into ASD behavior in dissolution media [12], the lateral spatial resolution is at least several micrometers (in contrast to sub-micron lateral spatial resolution for fluorescence imaging). Furthermore, since the sampling is immediately adjacent to the ASD-ATR crystal interface (within approximately 1 µm), the potential influence of the ATR crystal itself on the ASD behavior, that is not representative of the ASD more generally, needs to be kept in mind. Confocal Raman microscopy has the potential to fulfill the above criteria, and, depending on the setup, can offer a spatial resolution comparable to confocal fluorescence microscopy. Recently Krummnow *et al*. employed Raman line mapping to quantitatively image water-induced phase separation in amorphous solid dispersions during storage at different humidities, again using ritonavir and PVPVA ASDs as model systems [6]. Almost a decade earlier, Tres and coworkers [4] imaged drug loading dependent crystallization of felodipine in PVPVA ASDs in aqueous media with *in situ* confocal Raman microscopy. Both these studies involved analysis of the ASDs over a time scale of many hours, which allows the sufficient collection of the inherently weak spontaneous Raman scattering signal. These mapping times are too slow to capture fast-paced changes, within seconds or minutes, that can occur in aqueous media.

Non-linear optical (NLO) imaging techniques, such as stimulated Raman scattering (SRS) and coherent anti-Stokes Raman scattering (CARS) microscopy, are more advanced Raman-based imaging techniques that excel in rapid three-dimensional visualization of chemical and structural distributions of a sample at a sub-micrometer level of detail. Sum frequency generation (SFG), on the other hand, can complement coherent Raman microscopy by classifying any bulk structures as non-centrosymmetric crystals or amorphous/centrosymmetric crystals [13, 14]. The advent of modern NLO microscopy occurred in 1999 with the demonstration of Zumbusch et al of CARS microscopy [15], followed by a demonstration of SRS microscopy by Freudiger et al in 2008 [16]. In the last decade, SRS microscopy has become increasingly popular due to better spectral data and simpler user experience, namely the lack on non-resonant background signal and a linear concentration dependence.

CARS microscopy, sometimes augmented with SFG, has been used to image the distribution of API solid-state forms, as well as changes during storage and dissolution [17-19]. CARS and SRS have also been used to image API and excipient distributions in dosage forms (or intermediates) including tablets [20-22], extrudates [19, 23], films [24-26] and API-loaded mesoporous silica microparticles [27].

The first *in situ* analyses of dosage form changes during drug release involved CARS. Kang *et al*. imaged the distribution and release of paclitaxel from poly(ethyl-co-vinyl acetate) films in an isoporopyl alcohol-phosphate buffered saline solution [24-26]. CARS has also been used to image theophylline anhydrate release from lipid extrudates in water, as well as simultaneous theophylline monohydrate formation [19]. More recently, SRS microscopy has been used to image poly(D,L-lactic acid) extrudates as model implant formulations, in which particles of the API, entecavir, were distributed. SRS was employed to image the distribution of the two components, as well as the decrease in size and eventual disappearance of individual API particles during drug release in a flow through cell [23].

In this study, we employ SRS coupled with SFG for the first time for direct *in situ* nondestructive chemically-specific imaging of ASD behavior during drug release. Ritonavir (RTV) – polyvinyl pyrrolidone vinyl acetate (PVPVA) amorphous solid dispersion films at different drug-to-polymer ratios served as model systems. Different phenomena, including water penetration, amorphous-amorphous phase separation (AAPS), liquid-liquid phase separation (LLPS), and component release were imaged in real time. Furthermore, the phase separation was understood through the lens of both surface-directed and bulk phase separation.

Experimental Section

Materials

Ritonavir (thiazol-5-ylmethyl ((2S,3S,5S)-3-hydroxy-5-((S)-2-(3-((2-isopropylthiazol-4-yl)methyl)-3-methylureido)-3-methylbutanamido)-1,6-diphenylhexan-2-yl)carbamate (RTV), Figure 1 (left)) was supplied by BLD Pharm (China) in 99.87 % purity. Copovidone (vinylpyrrolidone-vinyl acetate copolymer with a vinylpyrrolidone to vinyl acetate ratio of 6:4 (PVPVA), Figure 1 (right)) was obtained under the brand name Kollidon® VA 64 from BASF SE (Ludwigshafen, Germany). Methanol (Emsure® for analysis ≥ 99.9 % purity) was supplied by Merck KGaA (Darmstadt, Germany). Phosphate buffer (pH 6.8, 100 mM) was prepared in-house using potassium dihydrogen phosphate (VWR Chemicals BDH®, Leuven, Belgium) and sodium hydroxide (Emsure® for analysis, Merck KGaA, Darmstadt, Germany).

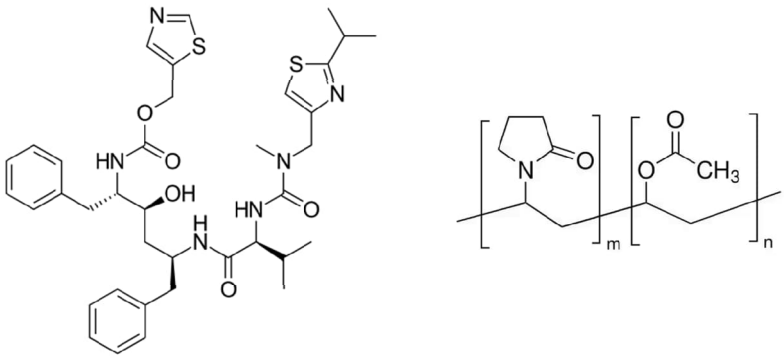

Figure 1. Molecular structures of RTV (left) and PVPVA 64 (right)

Methods

Film preparation

ASDs with different RTV to PVPVA ratios (at 20 % w/w intervals from 0 to 100 % drug loading) were prepared using solvent evaporation. Mixtures of RTV and PVPVA (total 1 g) were prepared at different RTV to PVPVA weight ratios (0:100, 20:80, 40:60, 60:40, 80:20 and 100:0) were prepared and dissolved in 5 mL of methanol (20 % w/v solid content) in 14 mL glass vials. The solutions were mixed using a vortex mixer and an ultrasonic bath sonicator (5 minutes) to ensure complete dissolution. The solutions were then cast onto a glass or aluminum substrate, depending on the subsequent analysis technique. The casting was performed in low humidity environment (20% relative humidity or less) to avoid immediate phase separation in the films. For X-ray powder diffraction (XRPD), polarizing light microscopy (PLM), and spontaneous Raman spectroscopy, 50 µl of each mixture was cast onto 18x18 mm square cover glasses (No. 1, EUKITT®, ORSAtec). For modulated temperature differential scanning calorimetry (mDSC), the solutions were cast directly into Tzero aluminum pans (TA Instruments, Switzerland). For SRS microscopy, ⌀35 mm glass bottom dishes with ⌀14 mm microwell and No. 1.5 cover glass (MatTek, USA) were used. A small droplet of the solution was cast onto the center of the microwell. All samples were then immediately placed in a vacuum oven at room temperature for approximately 44 hours for residual solvent removal and to prevent water sorption. Subsequently, the samples were stored in a dessicator over silica gel at room temperature until measurement.

X-ray powder diffraction

Diffractograms of the films were collected using a Rigaku SmartLab diffractometer (Rigaku, Japan) with Cu Kα radiation source and a HyPix-3000 detector. ASD films were gently scraped with a disposable scalpel and the scrapings were placed on a low-background sample holder (⌀5 x 0.2 mm) and scanned from 3 to 40° 2θ using a 2° min^{-1} scan rate and a step size of 0.01°.

Polarizing light microscopy

PLM was performed on the films (film side up) on 18x18 mm cover glasses with an Olympus BX50 Polarized Light Microscope (Olympus, Tokyo, Japan) equipped with Qimaging MicroPublisher 5.0 RTV (Real-Time Viewing) CCD Camera (QImaging, Canada) at 10x and 20x magnification.

Differential scanning calorimetry

Modulated differential scanning calorimetry (mDSC) was carried out using a Discovery DSC™ (TA Instruments, New Castle, DE, USA), equipped with a refrigerated cooling system (RCS90). Experiments were performed under dry nitrogen atmosphere at 50 mL/min flow rate, and the temperature was calibrated with pure indium. Tzero aluminum pans (TA Instruments, Switzerland) contained between 2 and 5 mg of each ASD that had previously been cast directly into the pans and vacuum dried. The pans were sealed with Tzero hermetic lids with pin holes (TA Instruments, USA). Thermal scans of raw materials and ASDs were acquired at a heating rate of 2 °C/min from -20 °C to 180 °C with a modulation of 1°C every 60 seconds.

Spontaneous Raman spectroscopy

Spontaneous Raman spectra of powder raw materials and prepared films with 0% and 100% drug loading were collected with a confocal Raman microscope (NT-MDT Ntegra Spectra, Russia) equipped with a 532 nm laser and 100x objective (Mitutoyo, Japan). The spectral range covered was from 300 to 3500 cm^{-1} with a resolution of approximately 10 cm^{-1} determined by measuring the full width of half maximum of the

Raman peak of silicon at 520.7 cm^{-1}. Powdered samples were placed on a microscope slide for the measurement, while the films were measured directly on the cover glasses they were prepared on. Laser power on the sample was 10 mW and the acquisition time was adjusted from 1 to 6 s depending on signal strength.

Nonlinear optical imaging

Nonlinear optical imaging, including SRS and SFG, was carried out with an in-house built microscope based on an Olympus FV3000 confocal laser scanning microscope (Olympus, Japan), and described in detail elsewhere [28]. The microscope system features an InSight X3+ (Spectra-Physics, USA) laser and a SF-TRU Timing and Recombination (Newport, USA) for fast hyperspectral SRS imaging [29]. Laser light was focused on the sample with an Olympus® UPLSAPO 60xW1600 objective and collected in transmission direction with a high NA condenser (Leica, Germany) immersed in the buffer medium if present. SRS signal was detected with an SRS detection module (APE Angewandte Physik und Elektronik GmbH, Germany) and SFG signal with a PMT1001 photomultiplier tube module (Thorlabs, Germany), separately. Instrument and experiment control was a combination of commercial FV31-SW software controlling the Olympus microscope frame, and in-house developed LabView (National Instruments, USA) based user interface controlling the nonlinear optical imaging instrumentation.

A schematic of the sampling setup for *in situ* imaging of the interaction of ASD with buffer is shown in Figure 2. The samples for SRS imaging were covered with a small, separately cut piece of cover glass (No. 1.5, EUKITT®, ORSAtec). The samples were then briefly heated from above using a hot air gun (Hot Air Rework Station CIF 852-A++, Farnell), allowing the top of the film to soften while gently pressing the cover glass down to adhere it to the film. This preparation method allowed the subsequently added buffer to penetrate only from the side of the film and not the top or bottom, such that the interaction of the ASD components perpendicular to the initial ASD-buffer interface could be imaged *in situ*.

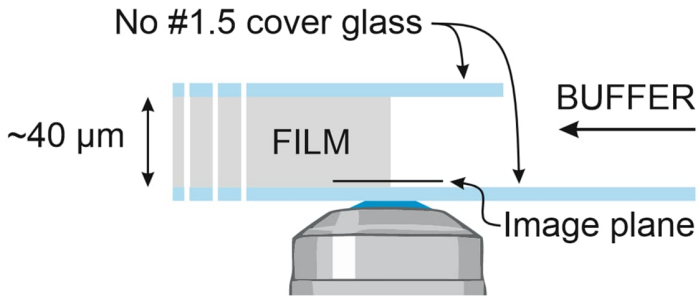

Figure 2. Schematic showing in situ imaging setup (not to scale)

Reflection imaging

Phase separation in the ASD films was also correlatively analyzed by simultaneously recording the reflected confocal signal from the same areas of the films using a 640 nm laser and the high sensitivity confocal GaAsP detectors of the FV3000 microscope with confocal aperture set to 306 µm.

Spectral data processing

The imaging data was analyzed and visualized with an in-house developed Matlab (MathWorks, USA) based application. The image sets were first filtered with BM4D, a state-of-the-art unsupervised noise reduction algorithm [30]. Measurements of pure and dry PVPVA and RTV films and pH 6.8 phosphate buffer were then used to generate reference spectra for non-negative classical least squares (CLS) unmixing analysis of the data obtained during the *in situ* analyses. For (semi-)quantitative analysis, the resulting CLS coefficients (scaling value of each reference spectra in a pixel) were scaled such that in each pixel the coefficients of the components (PVPVA, RTV, and buffer, depending on the measurement) sum to one (closure). Relative proportions of each component were calibrated using a known concentration location of a measurement and the calibration was the same for each dissolution experiment.

Results and discussion

Characterization of starting materials

Solid state characterization

XRPD of crystalline RTV starting material was consistent with the stable orthorhombic form II of RTV (Cambridge Structural Database (CSD) RefCODE YIGPIO01, space group $P2_12_12_1$). None of the films exhibited diffraction peaks indicative of crystallinity (Figure 3). Also, according to PLM analyses, the films prepared at all ratios were amorphous, homogeneous single-phase dispersions, and free of trace crystallinity (data not shown). DSC thermograms also suggested the ASDs were single phase systems, with each exhibiting a single glass transition temperature (T_g) progressively decreasing from 89.9 °C (midpoint) for 0% drug loading (100% PVPVA)) to 42.9 °C (midpoint) for 100% drug loading (Figure 4). These T_gs are slightly lower than the values reported by Krummnow et al [10] (at 325.99 K and 380.74 K for amorphous RTV and PVPVA respectively), probably due to different sample preparation conditions and/or measurement parameters.

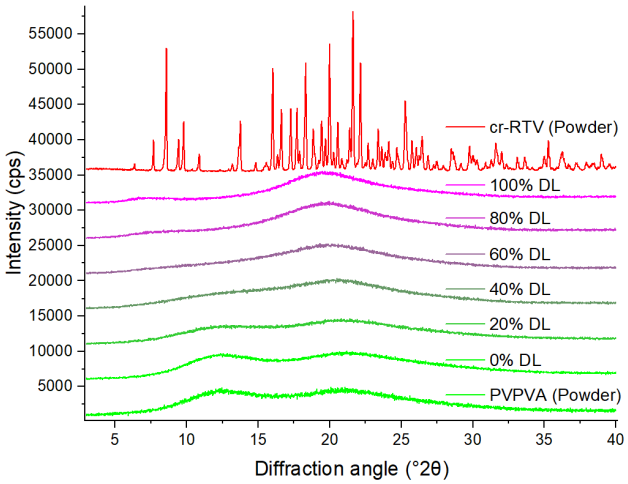

Figure 3. XRPD diffractograms of crystalline RTV and PVPVA powders as received, as well as ASD films with different drug loadings (DL, RTV:PVPVA w/w ratios).

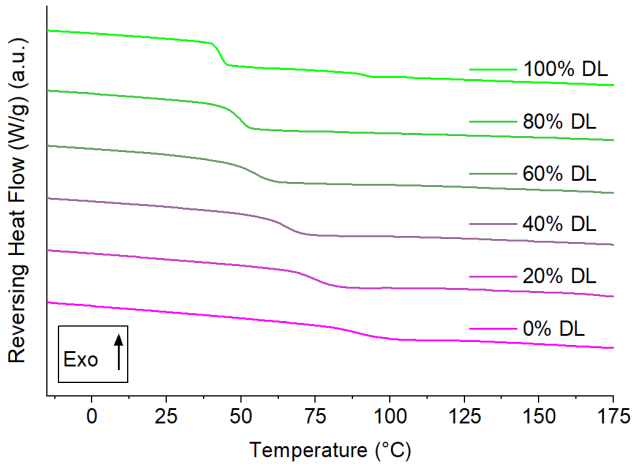

Figure 4. DSC thermograms of ASD films with different drug loadings (DL, RTV:PVPVA w/w ratios).

Spontaneous Raman spectroscopy

The Raman spectra of the crystalline and the amorphous pure drug film (Figure 5) are consistent with those previously presented between 600 and 1900 cm^{-1} for form II and the amorphous form of RTV [31], including a sharp peak at 1660 cm^{-1} (C=O stretching) characteristic for form II, which is much smaller and broadened for the amorphous form. We are not aware of published Raman spectra of RTV at higher frequencies, but the CH stretch region was also distinct for the two forms of RTV with peaks at 3059 cm^{-1} and 3097 cm^{-1} for the crystalline form and broader peaks centered at 2927 cm^{-1} and 3061 cm^{-1} for the amorphous form. In this region, PVPVA exhibited a peak at 2936 cm^{-1} and a pronounced shoulder at 2983 cm^{-1}.

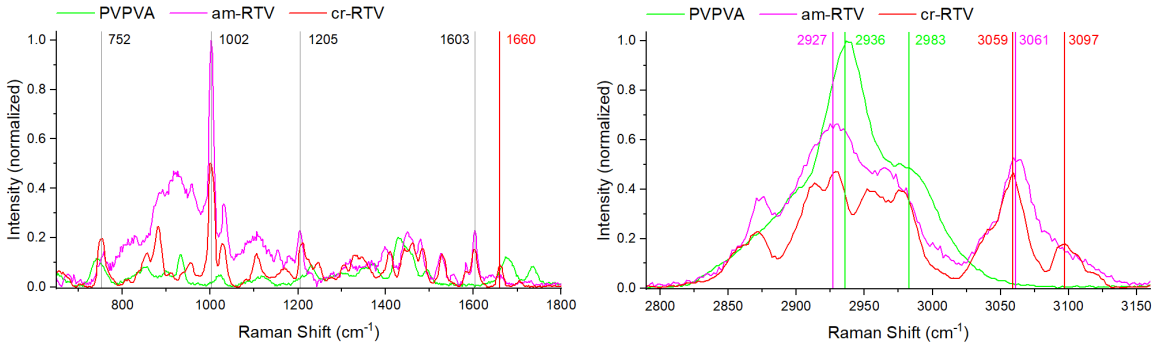

Figure 5. Spontaneous Raman spectra of crystalline RTV (cr-RTV), amorphous RTV (am-RTV) and PVPVA over the spectral ranges 650 cm^{-1} – 1800 cm^{-1} and 2790 cm^{-1} – 3160 cm^{-1}. Selected Raman shift positions characteristic of each of the components are marked.

Stimulated Raman scattering

Based on the spontaneous Raman spectra, the spectral region from 2850 to 3150 cm^{-1} was selected for SRS imaging of RTV and PVPVA. Additionally, the phosphate buffer signal (primarily water OH stretching) was recorded in this region. SRS spectra were recorded using two different spectral resolutions: high

resolution with a 6 cm^{-1} spectral step size and 51 spectral points in total (Figure 6, left), and low resolution with a 45 cm^{-1} spectral step size with 7 spectral points in total (Figure 6, right). The first reason for two different settings was optimization of the measurement speed based on requirements of *in situ* dissolution imaging: the lower resolution scan took about 10 seconds, whereas the higher resolution took about 60 seconds. The second reason was the reduction of the exposure to the laser illumination, which effectively reduces the chance for laser induced photodamage (burning). Faster measurements were used throughout each dissolution experiment and for the final timepoint an image with the high spectral resolution was recorded.

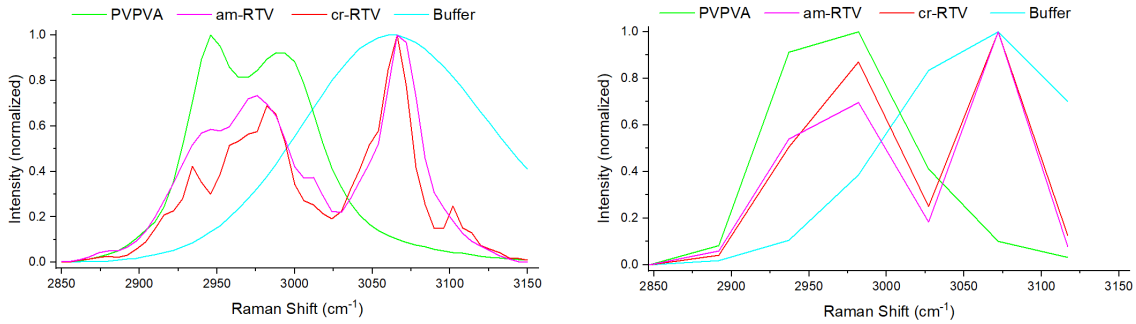

Figure 6. Stimulated Raman spectra of crystalline RTV (cr-RTV), amorphous RTV (am-RTV), PVPVA and buffer with high (left) and low (right) spectral resolution.

At high resolution (Figure 6, left), the spectra are distinct for each component and consistent with the corresponding spontaneous Raman spectra, except for the relative intensities of the spectral features — the SRS intensities towards the center of the spectral range are higher while those at the edges are diminished, when compared to the spontaneous Raman spectra. This difference is a consequence of the changing pulse overlap employed during spectral focusing (see Figure S1 in the Supporting Information for a pictorial explanation), causing a Gaussian-like intensity profile multiplying the spectra. The low-resolution spectra (Figure 6, right) are distinct for RTV, PVPVA and buffer, but cr-RTV and am-RTV are not clearly distinguishable. For this reason, correlative SFG together with the high-resolution spectra was additionally recorded at the end of each experiment to detect any RTV crystallization.

Correlative sum frequency generation (SFG)

The three polymorphs of RTV whose crystal structures have been published are the metastable monoclinic form I (space group $P2_1$, CSD RefCODE YIGPIO) [32], stable orthorhombic form II (space group $P2_12_12_1$, CSD RefCODE YIGPIO01) [32], and metastable monoclinic form III (space group C2, CSD RefCODE YIGPIO05) [31]. All three crystal structures are non-centrosymmetric and are thus capable of sustaining a SFG signal. Consistent with its non-centrosymmetric crystal structure, the crystalline RTV starting material, form II, exhibited SFG (Figure S2), while amorphous RTV, PVPVA and the buffer did not (data not shown). As such, SFG imaging was subsequently used as an indicator of any RTV crystallization in the films or dissolution media.

In situ imaging of films

Pure PVPVA and RTV films

We initially imaged the pure PVPVA and RTV films (0% and 100% drug loadings, respectively) as a function of buffer exposure time. Figure 7 shows the time-lapsed images of a neat PVPVA film before and after buffer addition (right), together with (semi-)quantitative analyses of the components from the

corresponding imaged areas (left). Initial qualitative interpretation of the CLS false color images (right), revealed that the film prior to buffer addition (0 min) had a sharp, clear interface between the homogenous PVPVA (green) and air (black, due to the sole presence of air). Upon buffer addition (cyan), polymer-buffer mixing was rapid and extensive, and the original interface disappeared already within 30 s. At this time point, the polymer signal (green color) dominated at the greatest depth in the film (bottom left corner of the image) and this gradually gave way to intense buffer signal (cyan) on the other side of the original interface (top-right corner of the image). The color became greener and more homogeneous in the imaged area over the next 5 min, indicating increased homogeneity with increasing PVPVA content, consistent with dissolution and diffusion of the polymer in the buffer.

The relative concentration distributions of PVPVA and buffer (or water) at each time point were analyzed (semi-)quantitatively using line plots (Figure 7, left). The average normalized CLS regression coefficients of the PVPVA and buffer signals at each position along the length of a rectangle normal to, and crossing over, the initial film-air interface are presented in (rectangles shown in the corresponding images on right Figure 7). As expected, before buffer addition, the PVPVA coefficients within the film are consistently at unity (representing pure PVPVA signal), and then immediately drop to 0 at the film-air interface and remain at 0 on the other side of the interface (due to the presence of air and absence of SRS signal). Within 30 s of buffer addition, the coefficients of both the PVPVA and buffer are both strongly represented either side of the original film-air interface, revealing substantial diffusion and mixing of the two components. Analysis of the buffer coefficients reveals that the waterfront had penetrated approximately 76 µm and 100 µm into the film after 0.5 min and 1 min respectively. The polymer concentration gradually decreases and water concentration increases at increasingly positive values on the *x*-axis, across the field of view, revealing continuous dissolution and diffusion of the polymer into the buffer and *vice versa*. These concentration gradients gradually decrease for both components as a function of time, revealing an increasingly homogeneous PVPVA-polymer solution across the imaged area. There are no abrupt changes in coefficient values at any point, and as such there is no evidence of the presence of a defined gel-solution interface.

The equivalent 100% RTV film time-lapsed images are shown in Figure 8. The dry film (0 min) was evenly magenta, and there was a sharp matrix-buffer interface, in a similar fashion to that observed for the polymer film. After addition of the buffer, in stark contrast to the PVPVA film, the RTV film appeared largely inert for the duration of the experiment, with the interface remaining at virtually the same position (now representing the RTV-buffer interface). The coefficient values of RTV and buffer were almost completely separate (most of the overlap can be attributed to an uneven interface, already evident from the RTV coefficient values at 0 min) and essentially unchanged for the entire imaging time (up to 30 min), indicating minimal mixing and dissolution of RTV. A very slight shift of the interface to the right at the latter time points suggests some very limited RTV film swelling (Figure 8). Correlative SFG analysis after 30 min additionally confirmed that the RTV remained amorphous (as evidenced through the absence of SFG signal, data not shown), consistent with previously published analyses of amorphous RTV after immersion in pH 6.8 buffer, as determined by *ex situ* Fourier-transform infrared (FTIR) spectroscopy and scanning electron microscopy (SEM) [33].

As would be expected for both the single-component films without the possibility for drug-polymer phase separation, the coefficients at each position along the *x*-axis have negligible standard deviations (not visible), across the entire analyzed area (in Figure 7 and Figure 8, for pure PVPVA and RTV films respectively).

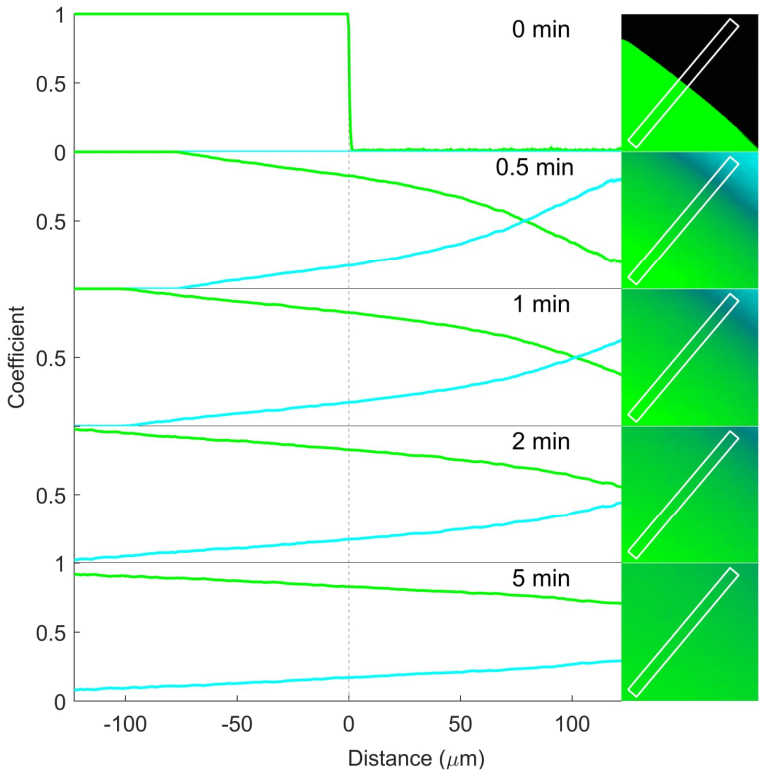

Figure 7. Relative concentration profiles of PVPVA (green) and pH 6.8 phosphate buffer (cyan) before (0 min) and 0.5, 1, 2 and 5 min after buffer addition to pure PVPVA film. Coefficients (representing relative concentration) along the *x*-axis are the mean (±SD) at each point along the marked rectangular region in the corresponding images to the right. The vertical dotted line at 0 µm represents the film-air interface before buffer addition (0 min). Due to the high degree of content homogeneity at each position along the rectangular region, the standard deviations are not visibly apparent.

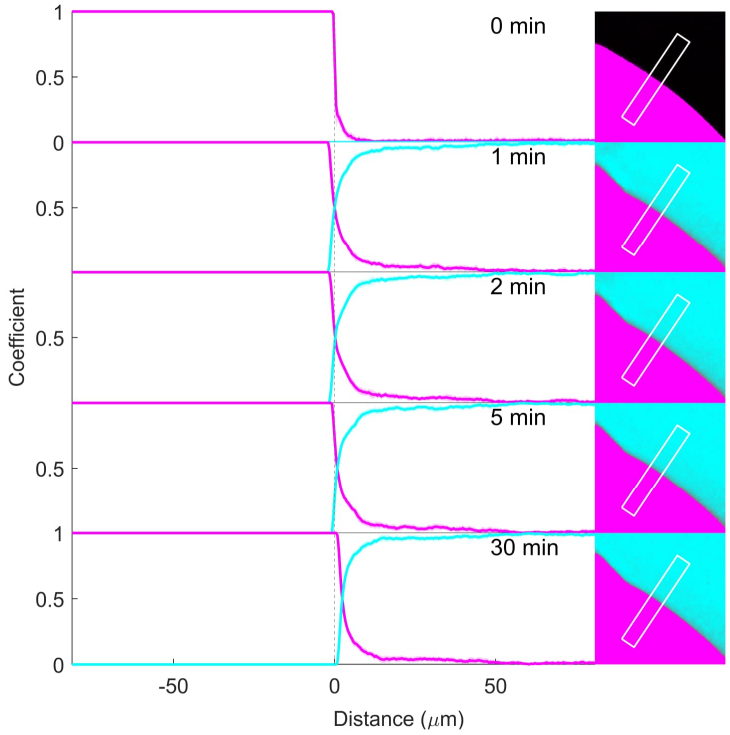

Figure 8. Relative concentration profiles of RTV (magenta) and pH 6.8 phosphate buffer (cyan) before (0 min) and 1, 2, 5, and 30 min after buffer addition to pure RTV film. Coefficients (representing relative concentration) along the *x*-axis are the mean (±SD) at each point along the marked rectangular region in the corresponding images to the right. The vertical dotted line at 0 µm represents the film-air interface before buffer addition (0 min) and at 1 min (as the sample was moved after the first image at 0 min due to sample burning). Due to the high degree of content homogeneity at each position along the rectangular region, the standard deviations are not visibly apparent.

RTV and PVPVA matrix films

Matrix films with drug loadings from 20 to 80 % were imaged *in situ* in the same manner as the single component films. However, the chemically-specific SRS imaging of these matrices was additionally complemented with correlative confocal reflection images, since the intensity and direction of elastic light scattering is sensitive to phase separation in multicomponent amorphous materials [34].

An absence of SFG signal in all samples (correlative SFG analysis was performed before and at the end of the *in situ* SRS analyses) confirmed the absence of any crystallization (data not shown) at all drug loadings, consistent with previous analyses of RTV-PVPVA ASDs films exposed to pH 6.8 buffer using ATR-FTIR spectroscopy [33].

20% drug loading

False-color SRS images of a film with 20% drug loading, together with the correlative grey-scale confocal reflection images of exactly the same areas, are presented in Figure 9 (right). At each time point, these images are complemented in the same figure with a coefficients plot on the left side of the figure, containing the chemically-specific SRS CLS coefficients (representing drug, polymer and buffer), as well as the correlative reflection coefficients (from exactly the same rectangular area). In the interpretation of the

data in Figure 9, first the chemically-specific SRS data is considered, followed by the correlative confocal reflection data.

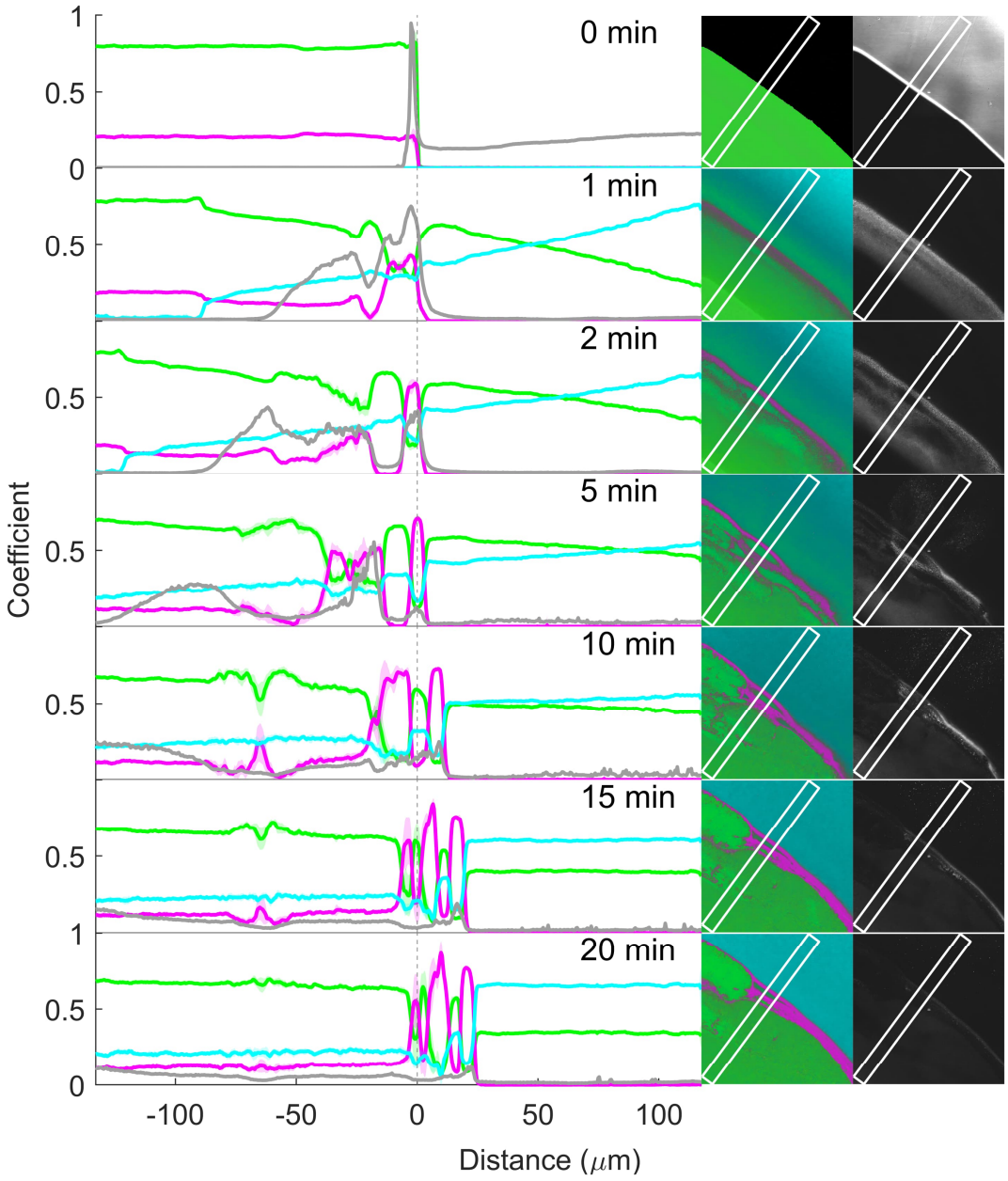

Figure 9. Coefficient (representing relative concentration) profiles of RTV (magenta), PVPVA (green) and pH 6.8 phosphate buffer (cyan), as well as confocal reflection intensity (gray), before (0 min) and 1, 2, 5, 10, 15 and 20 min after buffer addition to the matrix film with 20% drug loading. The coefficients along the *x*-axis are the mean (±SD for RTV, PVPVA and buffer) at each point along the marked rectangular region in the corresponding images to the right. The vertical dotted line at 0 µm represents the film-air interface before buffer addition (0 min).

The false color SRS image of the dry film (Figure 9, 0 minutes) was an almost uniform shade of green, consistent with a single-phase homogeneous film rich in PVPVA, and the film-air interface was sharp. The SRS coefficients measured from the rectangle in the image together with minimal standard deviations (not visible), are consistent with a homogenous distribution of 20% drug and 80% polymer across the film.

Upon buffer addition, the buffer (or water) signal in cyan color is visible towards the top right-hand corner of the images. Water penetration into the matrix resulted in an interface that is visible as a discrete change in shade of green towards the bottom left-hand corner of the SRS images at approximately 87 µm and 121 µm from the original interface at 1 and 2 min, respectively. The coefficients plot reveals that this represents the penetration of the water front into the film and therefore the glass-gel interface. At this interface, there is a discrete jump of water content from an undetectable level on the glassy side, to about 12% water content on the gel side, while the RTV and PVPVA coefficients correspondingly drop by approximately 5% and 7%, respectively. At later time points, this interface has penetrated further into the film beyond the field of view. The water penetration into the film and gel formation causes the film to gradually swell, with the matrix-buffer interface expanding into the buffer region by approximately 23 µm at the 20 min time point.

In the gel phase and dissolution medium, the water concentration continues to overall trend upwards and the polymer concentration trend downwards along the *x*-axis, for all time points up until and including 10 min, consistent with water penetration into the film and polymer dissolution into the buffer. However, there are strong concentration fluctuations in these upwards and downwards trends along the *x*-axis for the buffer and polymer, respectively. Furthermore, the RTV concentration coefficient shows opposing fluctuations in comparison to the polymer. These fluctuations in the gel are evidence of water-induced drug-polymer phase separation.

Already within 1 min of buffer exposure, drug-polymer phase separation has occurred, as evidenced in the false-color SRS images (Figure 9, second column from right) as drug-rich domains (pink) and polymer-rich domains (green). This is most visible in the false-color image as a thin magenta layer, along the location of the original film-air interface. Immediately to the right of drug-enriched interface, the polymer coefficients peak and gradually decrease to the right, deeper into the dissolution medium. Thus, as the hydrophilic and water-soluble polymer at the film surface preferentially associates with the buffer by dissolving and diffusing deeper into the dissolution medium, it leaves behind the hydrophobic drug which self-associates, enriches and forms a new interface matrix in the form of a drug enriched layer.

Inspection of the corresponding coefficients plot reveals that this drug-enriched layer at 1 min is approximately 10 µm wide, and in fact features two drug concentration maxima with a small drug concentration dip in between. Another, less intense, drug maximum is present at the *x*-axis position of approximately -26 µm. After 2 min, phase separation has intensified — the coefficients reveal sharper concentration differences between the drug rich and polymer rich layers. Later time points feature more layers of phase separation parallel to the original film-buffer interface. According to the coefficient plots, both the polymer and buffer coefficients consistently decrease together at the same positions where the drug coefficient increases. This can be attributed to the water preferably associating with the hydrophilic polymer over the hydrophobic drug. This finding is in line with observations of Krummnow et al (2023) [6], who used spontaneous Raman line-mapping microscopy to quantitatively image water-induced RTV and PVPVA phase separation in 20% and 25% drug loaded ASDs over several days at 94% relative humidity.

The false color images in Figure 9 also show that the water-induced surface-directed phase separation of drug and polymer (and water) within the ASD does not develop in a uniform manner parallel to the original film-buffer. This suggests the process is highly sensitive to experimental conditions, and presumably is also partially stochastic in nature. Nevertheless, the observations are consistent with the phenomenon of surface directed spinodal-decomposition, first experimentally reported by Jones et al (1991) [35] for unstable polymer blends in which one of the components has a preferential attraction to the surface. They observed composition wave vectors normal to and propagating inwards from the interface, maintaining coherence for several wavelengths.

In addition to surface-oriented phase separation, close inspection of the SRS false color images (Figure 9) reveals a second form of phase-separation within the films, namely water-induced *bulk* phase separation, which has previously been modelled in pharmaceutical PVPVA ASDs in buffer [6, 8, 10]. At the 20% drug loading, this manifests as the development of non-surface directed drug-rich (magenta) droplets within a continuous polymer-rich (green) network, consistent with previous indirect observation with confocal fluorescence microscopy involving fluorescent dyes [7, 8, 33], as well as thermodynamic perturbed-chain associating fluid theory (PC-SAFT) modelling [8, 10]. At 1 min, this is already observed in the SRS false color images on the microscale, with the phase separation appearing to extend deeper and deeper into the matrix after longer buffer exposure times. This can also be observed to some extent at 1 min as very fine oscillations in the polymer and drug coefficients between -50 µm and the surface-directed phase separation, and, as the domain sizes and concentration gradients grow (from 2 min onwards), also as increased coefficient standard deviations.

Since phase separation in both liquid and gel phases has been extensively studied with various light scattering techniques, such as dynamic light scattering [33], we further characterized the phase behavior in the gel phase of the film, as well as the dissolution medium, by employing correlative confocal reflection imaging with a 640 nm laser. While more advanced light scattering techniques can provide more comprehensive information, such as particle size on the nano- to micro-scale and density [33, 36-40], the confocal reflection imaging provides a simple approach to visualize the onset and propagation of phase separation (without chemical specificity) beyond the resolution limit of the chemically-specific SRS imaging. The resulting correlative reflection images are presented in greyscale in Figure 9 (far right column, representing exactly the same sample area as the false-color SRS images). Prior to buffer exposure, there is no significant reflection signal from the film (except for at the edge of the film), consistent with a single-phase film (outside the film area, the reflection signal from the glass/air interface disappears once the buffer is added). From 1 min onwards, the films exhibit a reflection response visible as grey/white regions in the grey-scale images in Figure 9 (right), indicative of nano- and micro-scale phase separation.

Comparison of the reflection and SRS coefficient plots (Figure 9, left) provides more detailed insight into phase separation in the gel as a function of film depth (negative x-position). In these plots, the reflection intensity from exactly the same positions as the SRS drug, polymer and buffer coefficients are presented (grey line). The reflection intensity distribution evolves over time. The initial onset of reflection intensity increase appears in the gel phase at approximately -60 µm, -84 µm and -128 µm at 1, 2 and 5 min, respectively (Figure 9). The increased reflection intensities appear as a 'wave' that gradually progresses deeper into the gel-phase of the film, and represent the first sign of nano- (and then micro-) phase separation. This phase separation front trails the water-front (glass-gel interface) by about 27 µm and 37 µm, at 1 and 2 min respectively. The elevated reflection signal appears earlier (deeper) in the gel phase than any chemically-specific SRS evidence of phase separation. This is because elastic scattering of light

already occurs with nano-scale phase separation below the applied sampling resolution of the SRS microscope in this experiment (approximated as three times the pixel size of 414 nm). Once the phase separation domain size has increased and is clearly evident with SRS, the elastic reflection signal intensity decreases. The minimum phase-separated domain size required to generate a detectable confocal reflection signal is not defined, but is likely on the order of tens of nanometers. As such, correlative non-chemically specific confocal reflection highly complements the chemically-specific SRS for *in situ* imaging of water-induced phase separation in ASD films. In the Supporting Information (Figure S4), a graphical representation of the evolution of three phenomena discussed above, namely the water penetration front (glass-gel interface, detected with SRS), phase separation front (detected with confocal reflection imaging), and matrix swelling (matrix-dissolution medium interface, detected with SRS), is presented (for the 20% drug loading, as well as higher drug loadings (*vida infra*)).

Liquid-liquid phase separation (LLPS), resulting in the presence of drug-rich droplets within the dissolution medium, has been widely reported for ASDs [36]. Upon close inspection of the SRS images (Figure 9), a very few drug rich droplets within the buffer-rich phase are visible from 5 min onwards (as magenta dots, highlighted with zoom in Figure S3). In this example, these are not of sufficient quantity and size to be represented as fluctuations in the drug coefficient line plot (with coefficient values remaining close to 0 throughout the buffer-rich phase). However, strong (non-chemically specific) evidence of nanodroplet formation in the buffer-rich phase (below the spatial resolution of the SRS microscope) is provided by the correlative confocal reflection images, in which localized reflections in the buffer-rich phase (white dots) are visible from 5 min onwards, together with clear oscillations in the reflection coefficients (Figure 9). A video of the movement of these nanodroplets is also present in the Supporting Information (Video S 1). Furthermore, in a separate example (*vide infra*) of a 20% drug loading film (replicate sample) after 30 min of buffer exposure, more pronounced LLPS with larger droplet sizes is clearly visible with SRS depth profiling (Figure 14).

Finally, 25 min after buffer addition and the film structural changes had slowed, we recorded an additional SRS image with high spectral resolution (Figure 10), together with the correlative reflection image. We directly compared four SRS spectra from different positions in the image, to reference SRS spectra of the amorphous RTV, PVPVA and buffer. The spectrum (yellow) at position 1 (yellow dot), is from a point where the confocal reflection data in Figure 9 suggested phase separation had occurred at around 5 min, but the SRS data suggested this phase separation was below the spatial resolution of the chemically-specific SRS imaging. This spectrum is most consistent with the reference PVPVA spectrum (peaks at approximately 2940 and 2990 cm^{-1}), but with a minority drug signal also present, as evidenced by the smaller peak at 3070 cm^{-1}. The spectrum from position 2 (bright green), representing the polymer enriched phase, is even more polymer-rich with the loss of the amorphous RTV peak. The spectrum from position 3 (magenta) is broadly consistent with amorphous RTV, with some minority PVPVA likely also contributing to the signal. The spectrum at position 4 is from the dissolution medium. This spectrum has spectral features consistent with both the polymer and buffer. Peak shifts relative to the reference PVPVA spectrum, consistent with hydrogen bonding between the polymer and water, are also apparent (approximately 3 cm^{-1} for positions 1 and 2, and 6 cm^{-1} for point 4, and could potentially be used as an additional characteristic to measure the hydration level of the polymer [41]). The SRS false-color image shows a single LLPS particle in the middle-right part of the buffer-rich region. The comparatively large pixel size employed, as well as constant movement of the particles, makes them more difficult to detect with hyperspectral SRS, whereas a large

number of LLPS particles (small bright dots in the buffer-rich region) is visible in the correlative reflection image.

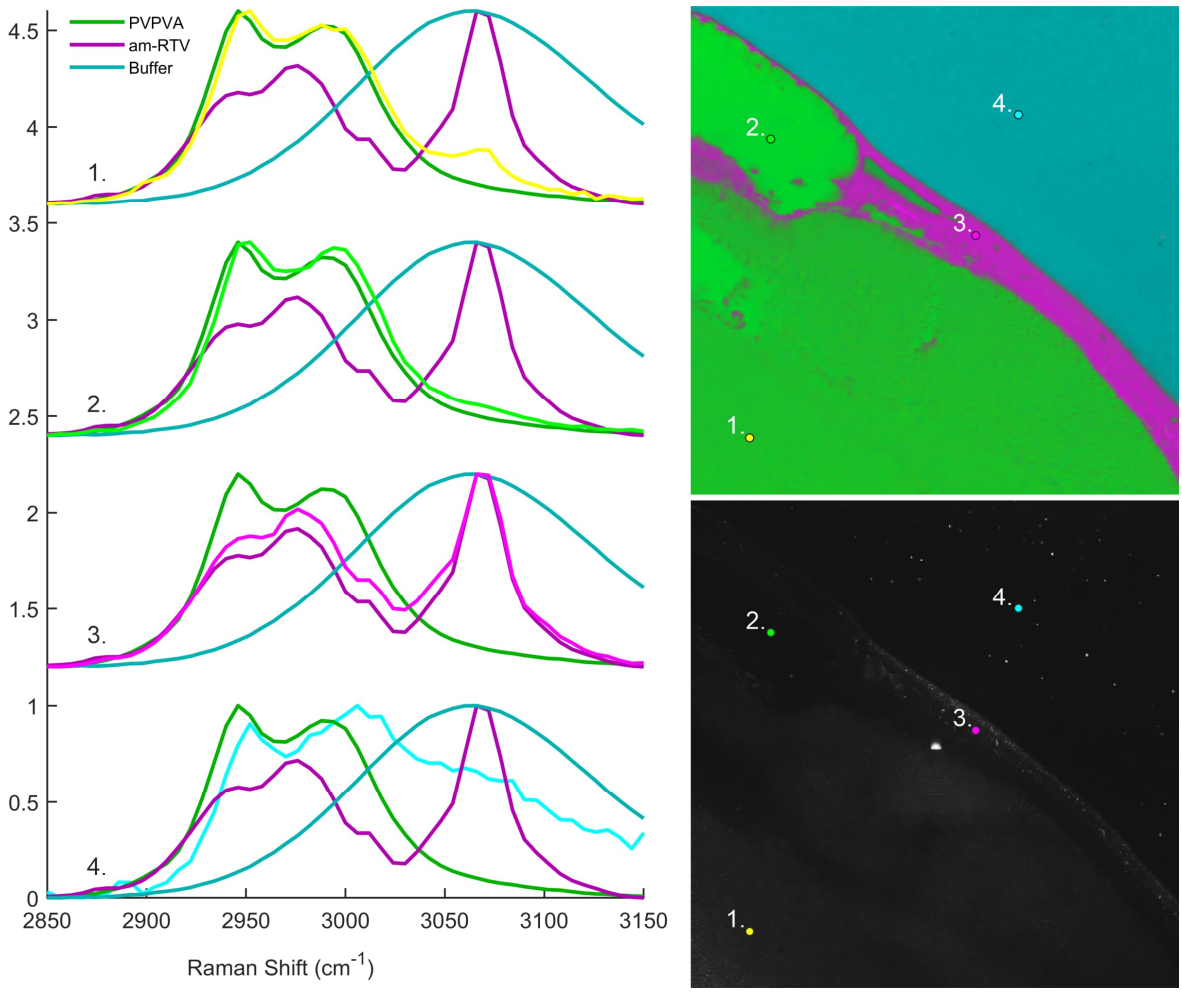

Figure 10. Example point spectra of RTV-PVPVA matrix film at 20% drug loading at the end of a dissolution experiment (time point 25 min after adding the phosphate buffer solution (pH 6.8)) (left). CLS reference spectra are labeled and shown in darker colors, while point spectra are shown in brighter color and their positions are indicated with numbered, colored dots in the false-color SRS (top right) and correlative reflection (bottom right) images. Image size 212x212 µm.

40% drug loading

The false color SRS images of 40% drug loading films, together with the respective correlative confocal reflection images for the are presented on the right in Figure 11, as well as the corresponding coefficients plots at each time point (left). Many of the same phenomena observed for the ASD film with 20% drug loading, were also observed at 40% drug loading, but they differed quantitatively.

The false color SRS image of the dry film (0 min) was an almost uniform shade of green, consistent with a single-phase homogeneous film richer in PVPVA than RTV, and the film-air interface was sharp. The green color was less rich than for the 20% drug loading, due to the larger contribution of RTV signal (magenta). The SRS coefficients extracted from the rectangle in the image together with minimal standard deviations (not visible), are consistent with a homogenous 40% drug and 60% polymer loading across the film.

Upon buffer addition, the buffer (or water) signal (cyan) is visible towards the top right-hand corner of the images. As with the 20% drug loading, the penetration of water into the matrix resulted in glass-gel interface that is visible as a discrete change in shade of green towards the bottom left-hand corner of the SRS false-color images, as well as the appearance of water signal in the corresponding coefficients plots. However, the water penetration was slower for the ASD with 40% drug loading than for the 20% drug loading, with the interface now appearing at approximately -68 µm and -90 µm from the original interface at 1 and 2 min, respectively (also see Figure S4, in the Supporting Information). In addition, the discrete increase of water content at this interface was slightly lower, at about 8%. At later time points, the glass-gel interface had again penetrated into the film beyond the field of view. Overall, compared to the 20% drug loading, the water concentration in the film is lower and, conversely, the polymer concentration in the buffer is also lower.

Rapid drug-polymer phase separation is also clearly evident for the 40% drug loading. Already within 1 min of buffer exposure, both *surface-directed* and *bulk* drug-polymer phase separation has occurred, with both drug-rich (pink) and polymer-rich (green) domains. Again, the water preferentially associated with the hydrophilic polymer (as revealed by the coefficients plots). At the 40% drug loading, the magenta drug signal is more prominent across the films, and at 1 min the drug layer at the surface is a few micrometers thicker, more uniform and with a higher peak drug concentration (about 70%) compared to the 20% drug loading. Once again, the phase separation intensifies over time, and surface-directed waves of alternating drug and polymer rich domains develop consistent with surface-directed spinodal decomposition. At 40% drug loading, the peak drug concentrations are greater and the drug rich-domains appear more continuous also within the matrix where bulk phase separation dominates.

The correlative confocal reflection images in Figure 11 (right, grey scale) and their corresponding reflection coefficients (grey line, Figure 11 left) reveal that once again, from 1 min onwards, the films again exhibit significant confocal reflection, consistent with nano- and micro-scale phase separation, that evolves within the films over time. Again, the reflection 'wave' in the gel phase gradually progresses deeper into the gel-phase of the film, albeit more slowly than for the 20% drug loading, with its onset position appearing in the gel phase at approximately -49 µm, -63 µm and -91 µm at 1, 2 and 5 min, respectively. This onset trails behind the glass-gel interface by about 19 µm and 27 µm, at 1 and 2 min, respectively (also see Figure S4, in the Supporting Information).

Interestingly, in this particular sample, mechanical strain on the phase-separated matrix is also evident. The polymer rich layer behind the drug-rich surface layer continues to expand up until 20 min, at which point it bursts through the drug layer, releasing most of the polymer and accompanied by a contraction of the matrix. Regardless of this mechanical disruption, overall, a significant amount of polymer was present in the buffer medium from 1 min onwards, while the drug signal was not detectable. Furthermore, in contrast to the 20% drug loading, neither SRS nor confocal reflection measurements suggested the presence of any (nano)droplet formation in the buffer-rich phase. These findings are broadly consistent with the earlier observations for ASDs of the same composition [7, 10, 33].

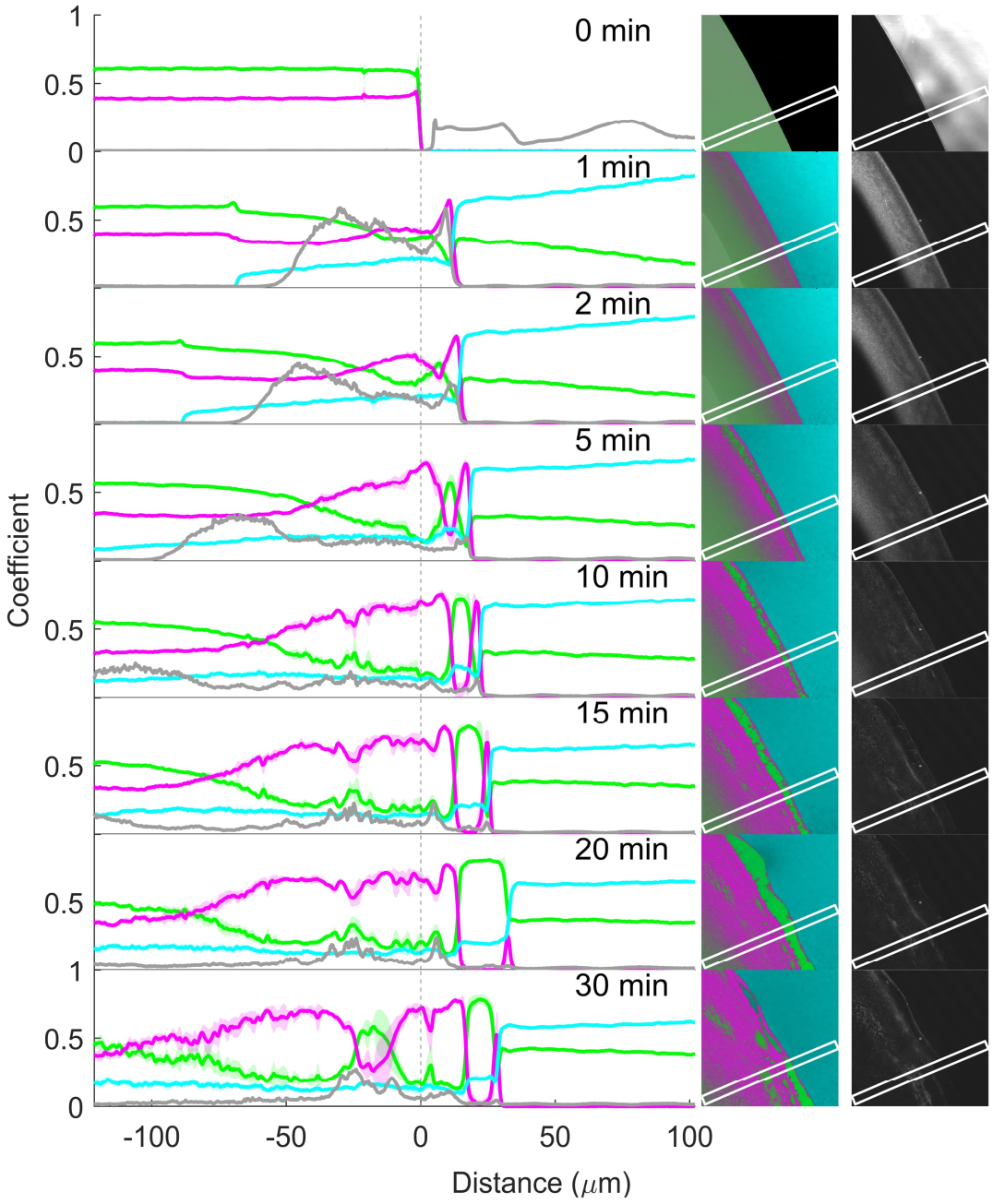

Figure 11. Coefficient (representing relative concentration) profiles of RTV (magenta), PVPVA (green) and pH 6.8 phosphate buffer (cyan), as well as confocal reflection intensity (gray), before (0 min) and 1, 2, 5, 10, 15, 20 and 30 min after buffer addition to matrix film with 40% drug loading. The coefficients along the x-axis are the mean (±SD for RTV, PVPVA and buffer) at each point along the marked rectangular region in the corresponding images to the right. The vertical dotted line at 0 µm represents the film-air interface before buffer addition (0 min).

60% drug loading

The false-color SRS image of the dry 60% drug loading film (0 min, Figure 12, right) was a largely uniform shade of pink, consistent with a single-phase homogeneous film richer in drug than polymer, as well as a sharp film-air interface. The corresponding SRS CLS coefficients (Figure 12, top left), extracted from the rectangle in the corresponding false color SRS image, are consistent with a homogenous 60% drug and 40% polymer loading across the film (a deviation of drug and polymer content of about 8% was observed within the film as a broad band in the film, but this does not affect the overall interpretation of phase changes). After buffer addition, the false-color SRS and correlative confocal reflection images at each time point, as well as the corresponding coefficients plots, broadly reveal several of the same phase change phenomena observed in the films with the 20% and 40% drug loadings, but with substantially different kinetics.

Upon buffer addition, a glass-gel interface, representing the water penetration front, is visible as a discrete change in the shade of color within the film (Figure 12, visible at 1, 2 and 5 min). The buffer coefficient values in the coefficients plots provide additional evidence of this water penetration front, also at the latter time points. The water penetration was, however, much slower for the ASD with 60% drug loading than for both the 20 and 40% drug loadings, with the penetration front appearing at approximately –17 µm, -27 µm, -42 µm, -55 µm, -76 µm, -84 µm and -94 µm from the original interface at 1, 2, 5, 10, 15, 20 and 30 min, respectively (also see Figure S4, in the Supporting Information). In addition to the slower water penetration, the buffer coefficient values suggest the water concentration in the gel was also lower across the gel phase at all time points, presumably due to the higher content of the hydrophobic drug. Water penetration was also associated with gradual film swelling up to approximately 18 µm after 30 min. Interestingly, the swelling is on the same order of magnitude as the lower drug loadings, and appears to be limited by the drug enriched matrix surface at all three drug loadings.

The SRS false color images and coefficients plots confirm that drug-polymer phase separation also occurs at the 60% drug loading, though somewhat more subtly in the SRS false color images. A continuous drug enriched surface layer is apparent already within 1 min of buffer exposure (visible in the 1 min SRS false color plot and SRS coefficient plot, Figure 12), accompanied by a few encapsulated polymer-rich pockets within this surface layer (1 min SRS false color image, Figure 12). These pockets gradually increases in size over the duration of the experiment. However unlike at the 40% drug loading, none of the imaged polymer pockets appear to break free from the continuous drug rich network at any point. Within the film, the reflection images clearly demonstrate bulk phase separation from the 1 min timepoint onwards and its continued propagation in the gel phase, trailing the water penetration front by approximately 3 µm at 1 min; this gap had expanded to approximately 44 µm after 30 min. The chemically-specific SRS false-color images reveal that this bulk phase separation within the film is characterized by a disperse polymer-rich phase within the continuous drug-rich phase.

Within the dissolution medium, the buffer signal is strongly visible and highly consistent (with the same shade of cyan) at all time points in the upper right-hand region of the false-color SRS images, suggesting the medium remains predominantly unchanged over time. Indeed, the buffer coefficient values in this region (positive values on the *x*-axis to the right of the matrix-dissolution medium interface) remained close to unity (representing 100%) at all times, while the polymer and drug coefficient values remained close to zero. Overall, this suggested negligible release of both the drug and the polymer at this drug loading, and can be attributed to the strong continuous drug-rich network within, and especially at the

surface, of the film. This network remains intact, despite some buffer penetration into the film and film swelling.

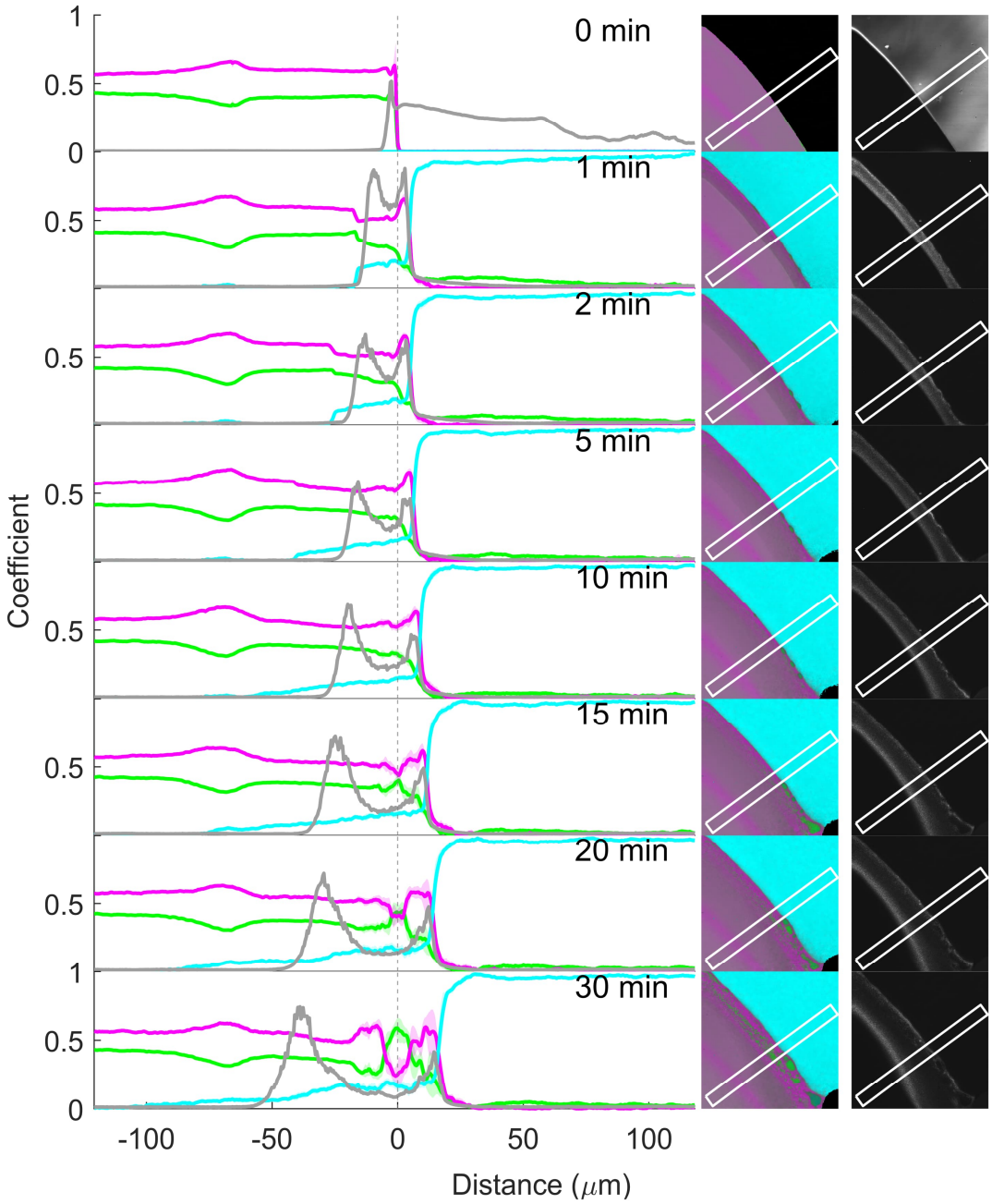

Figure 12. Coefficient (representing relative concentration) profiles of RTV (magenta), PVPVA (green) and pH 6.8 phosphate buffer (cyan), as well as confocal reflection intensity (gray), before (0 min) and 1, 2, 5, 10, 15, 20 and 30 min after buffer addition to matrix film with 60% drug loading. The coefficients along the x-axis are the mean (±SD for RTV, PVPVA and buffer) at each point along the marked rectangular region in the corresponding images to the right. The vertical dotted line at 0 µm represents the film-air interface before buffer addition (0 min).

80% drug loading

The analysis of the ASD with 80% drug loading is presented in Figure 13. The false color SRS image of the dry film (0 min) was an almost uniform shade of pink, consistent with a single-phase homogeneous film rich in PVPVA, and the film-air interface was sharp. The SRS coefficients extracted from the rectangle in the image together with minimal standard deviations (not visible), are consistent with a homogenous 80% and 20% drug and polymer loading across the film, respectively, with a sharp film-air interface. In contrast to all the ASDs with lower drug loadings, but consistent with the pure RTV film (Figure 8), this matrix appears essentially inert with no obvious chemical or physical changes to the film for the duration of the experiment (up to 30 min), including water penetration, swelling and phase separation, and no drug or polymer release into the buffer.

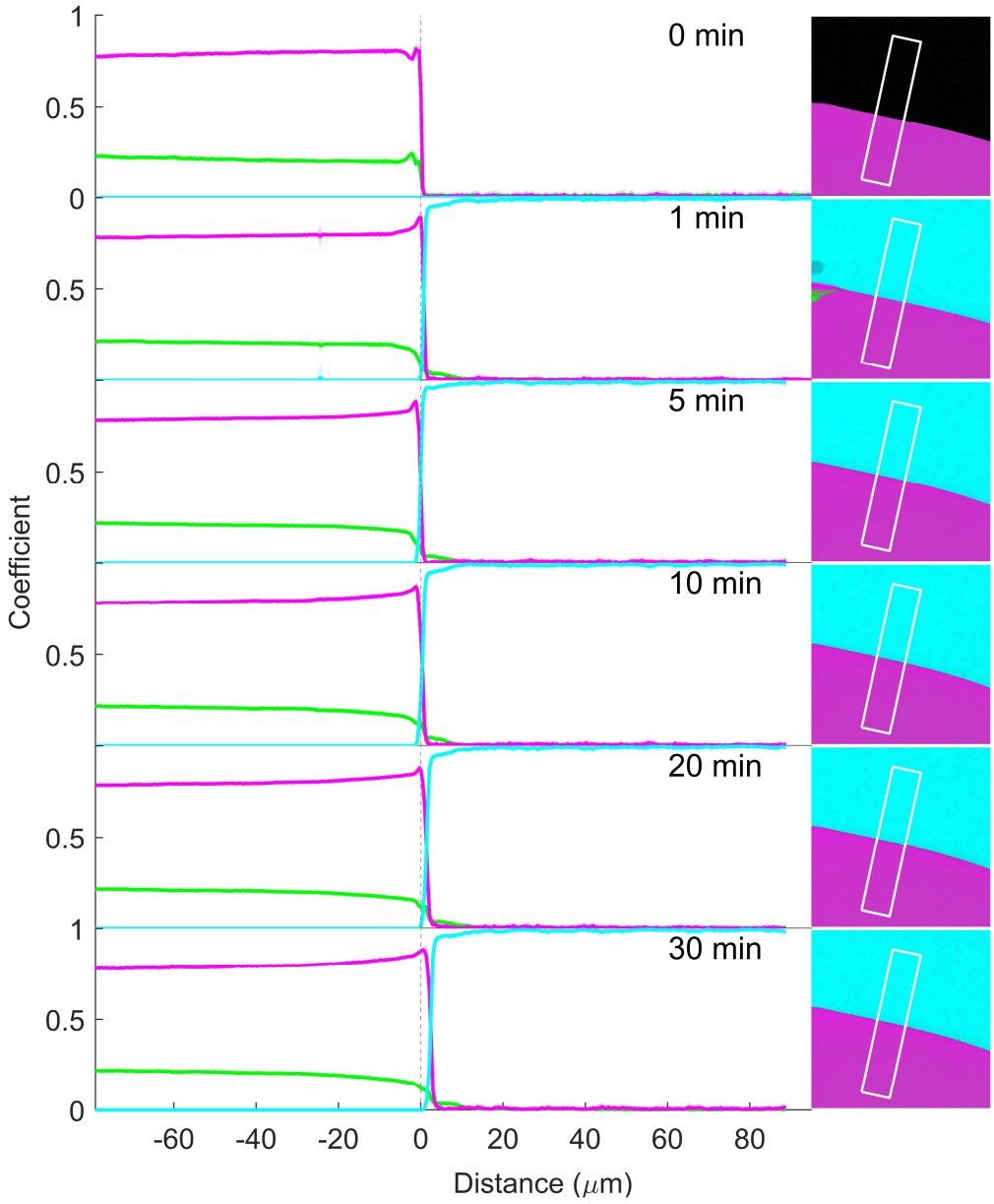

Figure 13. Coefficient (representing relative concentration) profiles of RTV (magenta), PVPVA (green) and pH 6.8 phosphate buffer (cyan), before (0 min) and 1, 2, 5, 10, 15, 20 and 30 min after buffer addition to matrix film with 80% drug loading. The coefficients along the x-axis are the mean (±SD for RTV, PVPVA and buffer) at each point along the marked rectangular region in the corresponding SRS images to the right. The vertical dotted line at 0 µm represents the film-air interface before buffer addition (0 min). The sampled area was moved prior to the 5 min image due to sample burning. Due to the high degree of content homogeneity at each position along the rectangular region, the standard deviations are not visibly apparent.

Depth profiling of matrix film

We also investigated phase separation as a function of sampling depth. For this, we recorded images at different depths over a total depth range of 22 µm within a 20% drug loaded film (replicate experiment)

at the 30 min timepoint (Figure 14). The images reveal significantly different distributions as a function of sampling depth. At the top and bottom imaging depths, in the vicinity of the glass cover slips, near continuous drug rich domains are observed, suggesting that the drug has preferentially phase separated toward the glass during water penetration, while the polymer has concentrated towards the middle of the film. Four planes at different depths are also shown in Figure 14 (top). While phase separation is evident at each of these layers, the layers near the top and bottom (closest to the glass cover slips) show more bicontinuous drug and polymer domains across large sections of the image matrix area, while in the middle of the layer, the drug rich phase is more predominantly represented by discrete droplets in a continuous polymer-rich phase with the continuous drug layer being restricted to the matrix-buffer interface. These substantially different observations highlight the importance of sampling setup, and in this case in particular, being aware of the potential of glass-matrix interfaces introducing artefacts into the observed phase behavior. In our studies, we have by default imaged the film close to coverslip closest to the microscope objective to maximize spatial resolution and signal strength and therefore image quality (the detrimental effect of sampling depth on image quality is evident from the four planes shown in Figure 14). However, these effects should be kept in mind, when interpreting the images with different drug loadings.

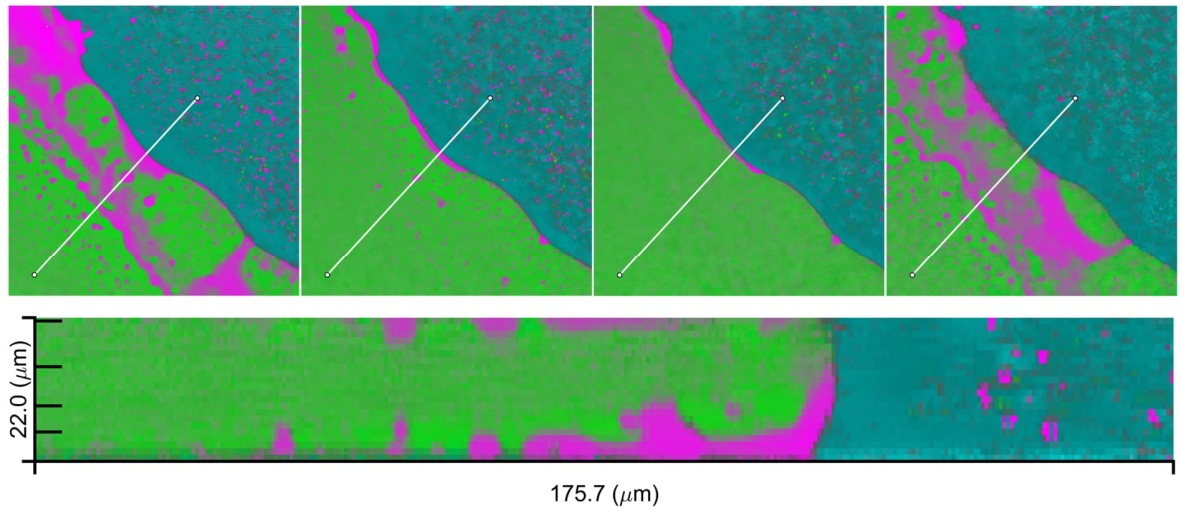

Figure 14. 3D visualization of a matrix film at 20% drug loading (replicate experiment) past 30 min after buffer addition, with RTV (magenta), PVPVA (green) and pH 6.8 phosphate buffer (cyan). Cross-section view in the lower image for the line shown in the images above, with the images above representing normal XY plane sections. The drug-rich phase is more pronounced in the top and bottom frames, close/at the glass interfaces. The image stack height is 22 µm and the presented images are organized from bottom (far left) to top (far right) from left to right at distances of 4, 8, 12 and 21 µm from the bottom.

Limit of congruence

In considering the congruency of drug and polymer release, our SRS (semi-)quantitative imaging of the buffer-rich phase with the 20 wt% and 40 wt% drug loadings, suggests that the drug and polymer do not release congruently (i.e. proportionately), with significant polymer release and an apparent drug concentration in the buffer well below the 20:80 wt% and 40:60 wt% drug-to-polymer ratios, respectively (at 60 and 80% wt% drug loadings, neither drug nor polymer release was readily detectable).

The lack of congruent release at 20 wt% drug loading, is in contrast to the results of Indulkar et al and Yang et al [7, 33], who obtained congruent release for RTV-PVPVA ASDs in pH 6.8 buffer at 20% drug loading (based on HPLC analysis of the dissolution medium), and identified the limit of congruency to be approximately 25% RTV loading. However, substantial experimental and sampling differences were present between their and our setups, including compacts vs film, different dissolution setup geometries and flow dynamics (including stirring vs no stirring), and 37 °C vs room temperature. Evidence that temperature significantly alters the congruence limit already exists, as Krummnow et al [10], who also investigated phase separation and release from spray-dried RTV-PVPVA ASDs at 25 °C (in stirred pH 7 dissolution medium and using UV detection), observed incongruent and disproportionately low drug release already at 20 wt% drug loading. This is in line with our observations. More generally, we also need to emphasize that our (semi-)quantitative analyses were not validated, and peak position shifts of the PVPVA signal in the film *versus* buffer phases (Figure 10) could have affected relative concentration predictions in the buffer rich phase.

Our results are in line, however, with surface-oriented phase separation involving the development of the (semi-)continuous drug rich-layer that we observed with *in situ* SRS imaging. Indulkar et al and Yang et al [7, 33] attributed their observed congruent release at 20% drug loading with the lack of the development of a continuous drug rich layer at the film-buffer interface, which they determined using ATR-FTIR spectroscopy, SEM and confocal fluorescence microscopy with marker dyes. Therefore, the drug release results for both their and our studies are consistent, considering the influence of the development of a drug-rich layer at the film-polymer interface. Despite this, it was interesting to note that we nevertheless still observed LLPS and nanodroplet formation at 20%, even with the surface enrichment of the drug. This suggests that surface enrichment and LLPS are not necessarily mutually exclusive.

Conclusions

In this study, we have demonstrated the application of SRS microscopy, augmented with SFG and confocal reflection measurements, for label-free and chemically-specific imaging of fast-paced phase changes in ASDs exposed to aqueous media. We were able to (semi-)quantify the drug, polymer and water distributions, both within the films and the dissolution medium. Phase phenomena that were imaged in real time include the water penetration front (representing the glass-gel interface), matrix swelling, dissolution, bulk and surface-directed AAPS within the film (including surface enrichment of the drug), and LLPS within the dissolution medium. These phenomena were strongly affected by drug loading. Overall, SRS microscopy with fast spectral focusing is well suited for qualitative and quantitative insights into water-induced ASD phase phenomena, with chemical, solid-state, temporal and spatial resolution. These insights should facilitate ASD formulation development, especially since there is potential for quantitative imaging of more chemically complex ASDs containing multiple APIs and/or excipients.

Supporting information

Supporting information.pdf: Additional experimental details, materials, and methods.

B20 disso1 site_0003.av1: Video of confocal reflection signal of from RTV-PVPVA film in pH 6.8 buffer ASD at 20% drug loading, revealing the presence and movement of nanodroplets.

Acknowledgements

The Quantitative Chemically-Specific Imaging Infrastructure for Material and Life Sciences (qCSI), University of Helsinki, was utilized in this research. The authors thank Tarja Katisko, Anniina Rummukainen and Kirsi Salomäki for assistance with the XRPD, DSC and PLM measurements. Funding: This work was supported, in part by Tandem Industry Academia Professor funding from the Finnish Research Impact Foundation (decision number 392) and the Research Council of Finland (project Nos. 331837 and 327732).

Conflict of Interest Disclosure

The authors declare no competing financial interest.

Abbreviations

Amorphous-amorphous phase separation (AAPS); amorphous solid dispersion (ASD); coherent anti-Stokes Raman scattering (CARS); co-povidone (PVPVA); differential scanning calorimetry (DSC); ritonavir (RTV); polarising light microscopy (PLM); stimulated Raman scattering (SRS); sum frequency generation (SFG); X-ray powder diffraction (XRPD)

References

(1) Shah, N., Sandhu, H., Choi, D. S., Chokshi, H., Malick, A.W. Amorphous Solid Dispersions. In *Advances in Delivery Science and Technology*, 1 ed.; Springer New York: New York, p 699.

(2) Schittny, A.; Huwyler, J.; Puchkov, M. Mechanisms of increased bioavailability through amorphous solid dispersions: a review. *Drug Deliv.* 2020, *27* (1), 110-127.

(3) Laitinen, R.; Priemel, P. A.; Surwase, S.; Graeser, K.; Strachan, C. J.; Grohganz, H.; Rades, T. Theoretical Considerations in Developing Amorphous Solid Dispersions. In *Amorphous Solid Dispersions: Theory and Practice*, Shah, N., Sandhu, H., Choi, D. S., Chokshi, H., Malick, A. W. Eds.; Springer New York, 2014; pp 35-90.

(5) Punčochová, K.; Ewing, A. V.; Gajdošová, M.; Pekárek, T.; Beránek, J.; Kazarian, S. G.; Štěpánek, F. The combined use of imaging approaches to assess drug release from multicomponent solid dispersions. *Pharm. Res.* 2017, *34* (5), 990-1001.

(6) Krummnow, A.; Danzer, A.; Voges, K.; Kyerematen, S. O.; Degenhardt, M.; Sadowski, G. Kinetics of water-induced amorphous phase separation in amorphous solid dispersions via Raman mapping. *Pharmaceutics* 2023, *15* (5), 1395.

(7) Yang, R.; Zhang, G. G. Z.; Zemlyanov, D. Y.; Purohit, H. S.; Taylor, L. S. Release mechanisms of amorphous solid dispersions: Role of drug-polymer phase separation and morphology. *J. Pharm. Sci.* 2023, *112* (1), 304-317.

(8) Deac, A.; Luebbert, C.; Qi, Q.; Courtney, R. M.; Indulkar, A. S.; Gao, Y.; Zhang, G. G. Z.; Sadowski, G.; Taylor, L. S. Dissolution mechanisms of amorphous solid dispersions: Application of ternary phase diagrams to explain release behavior. *Pharmaceutics* 2024, *21* (4), 1900-1918.

(9) Deac, A.; Qi, Q.; Indulkar, A. S.; Purohit, H. S.; Gao, Y.; Zhang, G. G. Z.; Taylor, L. S. Dissolution mechanisms of amorphous solid dispersions: Role of drug load and molecular interactions. *Pharmaceutics* 2023, *20* (1), 722-737.

(10) Krummnow, A.; Danzer, A.; Voges, K.; Dohrn, S.; Kyerematen, S. O.; Degenhardt, M.; Sadowski, G. Explaining the release mechanism of ritonavir/PVPVA amorphous solid dispersions. *Pharmaceutics* 2022, *14* (9), 1904.

(11) Han, Y. R.; Ma, Y.; Lee, P. I. Impact of phase separation morphology on release mechanism of amorphous solid dispersions. *Eur. J. Pharm. Sci.* 2019, *136*, 104955.

(12) van Haaren, C.; De Bock, M.; Kazarian, S. G. Advances in ATR-FTIR spectroscopic imaging for the analysis of tablet dissolution and drug release. *Molecules* 2023, *28* (12), 4705.
(13) Strachan, C. J.; Lee, C. J.; Rades, T. Partial characterization of different mixtures of solids by measuring the optical nonlinear response. *J. Pharm. Sci.* 2004, *93* (3), 733-742.
(14) Wanapun, D.; Kestur, U. S.; Kissick, D. J.; Simpson, G. J.; Taylor, L. S. Selective detection and quantitation of organic molecule crystallization by second harmonic generation microscopy. 2010, *82* (13), 5425-5432.
(16) Freudiger, C. W.; Min, W.; Saar, B. G.; Lu, S.; Holtom, G. R.; He, C.; Tsai, J. C.; Kang, J. X.; Xie, X. S. Label-free biomedical imaging with high sensitivity by stimulated Raman scattering microscopy. *Science* 2008, *322* (5909), 1857-1861.
(17) Novakovic, D.; Isomäki, A.; Pleunis, B.; Fraser-Miller, S. J.; Peltonen, L.; Laaksonen, T.; Strachan, C. J. Understanding dissolution and crystallization with imaging: A surface point of view. *Pharmaceutics* 2018, *15* (11), 5361-5373
(18) Novakovic, D.; Saarinen, J.; Rojalin, T.; Antikainen, O.; Fraser-Miller, S. J.; Laaksonen, T.; Peltonen, L.; Isomäki, A.; Strachan, C. J. Multimodal nonlinear optical imaging for sensitive detection of multiple pharmaceutical solid-state forms and surface transformations. 2017, *89* (21), 11460-11467.
(19) Windbergs, M.; Jurna, M.; Offerhaus, H. L.; Herek, J. L.; Kleinebudde, P.; Strachan, C. J. Chemical imaging of oral solid dosage forms and changes upon dissolution using coherent anti-Stokes Raman scattering microscopy *Anal. Chem.* 2009, *81* (6), 2085–2091.
(20) Slipchenko, M. N.; Chen, H.; Ely, D. R.; Jung, Y.; Carvajal, M. T.; Cheng, J.-X. Vibrational imaging of tablets by epi-detected stimulated Raman scattering microscopy. *Analyst* 2010, *135* (10).
(21) Ojarinta, R.; Saarinen, J.; Strachan, C. J.; Korhonen, O.; Laitinen, R. Preparation and characterization of multi-component tablets containing co-amorphous salts: Combining multimodal non-linear optical imaging with established analytical methods. *European Journal of Pharmaceutics and Biopharmaceutics* 2018, *132*, 112-126.
(22) Figueroa, B.; Nguyen, T.; Sotthivirat, S.; Xu, W.; Rhodes, T.; Lamm, M. S.; Smith, R. L.; John, C. T.; Su, Y.; Fu, D. Detecting and quantifying microscale chemical reactions in pharmaceutical tablets by stimulated Raman scattering microscopy. *Anal. Chem.* 2019, *91* (10), 6894-6901.
(23) Francis, A. T.; Nguyen, T. T.; Lamm, M. S.; Teller, R.; Forster, S. P.; Xu, W.; Rhodes, T.; Smith, R. L.; Kuiper, J.; Su, Y.; et al. In situ stimulated Raman scattering (SRS) microscopy study of the dissolution of sustained-release implant formulation. *Mol. Pharmaceutics* 2018, *15* (12), 5793-5801.
(24) Kang, E.; Robinson, J.; Park, K.; Cheng, J. X. Paclitaxel distribution in poly(ethylene glycol)/poly(lactide-co-glycolic acid) blends and its release visualized by coherent anti-Stokes Raman scattering microscopy. *J. Control. Release* 2007, *122* (3), 261-268.
(25) Kang, E.; Wang, H.; Kwon, I. K.; Song, Y.-H.; Kamath, K.; Miller, K. M.; Barry, J.; Cheng, J.-X.; Park, K. Application of coherent anti-stokes Raman scattering microscopy to image the changes in a paclitaxel–poly(styrene-b-isobutylene-b-styrene) matrix pre- and post-drug elution. *J. Biomed. Mat. Res. Part A* 2008, *87A* (4), 913-920.
(26) Kang, E. N.; Wang, H. F.; Kwon, I. K.; Robinson, J.; Park, K.; Cheng, J. X. In situ visualization of paclitaxel distribution and release by coherent anti-stokes Raman scattering microscopy. *Anal. Chem.* 2006, *78* (23), 8036-8043.
(27) Fussell, A. L.; Mah, P. T.; Offerhaus, H.; Niemi, S. M.; Salonen, J.; Santos, H. A.; Strachan, C. Coherent anti-Stokes Raman scattering microscopy driving the future of loaded mesoporous silica imaging. *Acta Biomater.* 2014, *10* (11), 4870-4877.
(28) Tomberg, T.; Isomäki, A.; Vainio, M.; Metsälä, M.; Saarinen, J.; Strachan, C. Multimodal nonlinear optical microscope for material and life sciences. *Optics Continuum* 2024, *In press*. DOI: https://doi.org/10.1364/OPTCON.532676.
(29) Zeytunyan, A.; Baldacchini, T.; Zadoyan, R. *Module for multiphoton high-resolution hyperspectral imaging and spectroscopy*; SPIE, 2018.

(30) Maggioni, M.; Katkovnik, V.; Egiazarian, K.; Foi, A. Nonlocal transform-domain filter for volumetric data denoising and reconstruction. *IEEE Transactions on Image Processing* 2013, *22* (1), 119-133.
(31) Yao, X.; Henry, R. F.; Zhang, G. G. Z. Ritonavir form III: A new polymorph after 24 years. *J. Pharm. Sci.* 2023, *112* (1), 237-242.
(32) Bauer, J.; Spanton, S.; Henry, R.; Quick, J.; Dziki, W.; Porter, W.; Morris, J. Ritonavir: an extraordinary example of conformational polymorphism. *Pharm. Res.* 2001, *18* (6).
(33) Indulkar, A. S.; Lou, X.; Zhang, G. G. Z.; Taylor, L. S. Insights into the dissolution mechanism of ritonavir–copovidone amorphous solid dispersions: Importance of congruent release for Enhanced performance. *Mol. Pharmaceutics* 2019, *16* (3), 1327-1339.
(34) Andreev, N. S. Scattering of visible light by glasses undergoing phase separation and homogenization. *J. Non-Crystalline Solids* 1978, *30* (2), 99-126.
(35) Jones, R. A. L.; Norton, L. J.; Kramer, E. J.; Bates, F. S.; Wiltzius, P. Surface-directed spinodal decomposition. *Phys. Rev. Lett.* 1991, *66* (10), 1326-1329.
(36) Zhao, P.; Han, W.; Shu, Y.; Li, M.; Sun, Y.; Sui, X.; Liu, B.; Tian, B.; Liu, Y.; Fu, Q. Liquid–liquid phase separation drug aggregate: Merit for oral delivery of amorphous solid dispersions. *J. Control. Release* 2023, *353*, 42-50.
(37) Morozova, S.; Hitimana, E.; Dhakal, S.; Wilcox, K. G.; Estrin, D. Scattering methods for determining structure and dynamics of polymer gels. *J. Appl.Phys.* 2021, *129* (7).
(38) Shibayama, M.; Norisuye, T. Gel formation analyses by dynamic light scattering. *Bull. Chem. Soc. Jpn* 2002, *75* (4), 641-659.
(39) Scheffold, F.; Cerbino, R. New trends in light scattering. *Curr. Opin. Colloid Interface Sci.* 2007, *12* (1), 50-57.
(40) Maguire, C. M.; Rösslein, M.; Wick, P.; Prina-Mello, A. Characterisation of particles in solution – a perspective on light scattering and comparative technologies. *Sci. Technol. Adv. Mater.* 2018, *19* (1), 732-745.
(41) Taylor, L. S.; Langkilde, F. W.; Zografi, G. Fourier transform Raman spectroscopic study of the interaction of water vapor with amorphous polymers. *J. Pharm. Sci.* 2001, *90* (7), 888-901.